Microcellular Poly(hydroxybutyrate-*co*-hydroxyvalerate)-Hyperbranched Polymer–Nanoclay Nanocomposites

Alireza Javadi,[1,2] Yottha Srithep,[3] Srikanth Pilla,[4] Craig C. Clemons,[5] Shaoqin Gong,[1,2] Lih-Sheng Turng[2,3]

[1] *Department of Biomedical Engineering, University of Wisconsin–Madison, WI*

[2] *Wisconsin Institute for Discovery, Madison, WI*

[3] *Department of Mechanical Engineering, University of Wisconsin–Madison, WI*

[4] *Department of Civil and Environmental Engineering, Stanford University, CA*

[5] *Forest Products Laboratory, United States Department of Agriculture, Madison, WI*

The effects of incorporating hyperbranched polymers (HBPs) and different nanoclays [Cloisite® 30B and halloysite nanotubes (HNT)] on the mechanical, morphological, and thermal properties of solid and microcellular poly(hydroxybutyrate-*co*-hydroxyvalerate) (PHBV) were investigated. According to the X-ray diffraction (XRD) and transmission electron microscopy (TEM) analyses, Cloisite 30B exhibited a combination of exfoliation and heterogeneous intercalation structure for both solid and microcellular PHBV–12% HBP–2% Cloisite 30B nanocomposites. TEM images indicated that HNTs were uniformly dispersed throughout the PHBV matrix. The addition of 2% nanoclays improved the thermal stability of the resulting nanocomposites. The addition of HBP+poly(maleic anhydride-*alt*-1-octadecene) (PA), Cloisite 30B, and HNT reduced the average cell size and increased the cell density of the microcellular components. The addition of (HBP+PA), Cloisite 30B, and HNT also increased the degree of crystallinity for both solid and microcellular components in comparison with neat PHBV. Also, with the addition of 12% (HBP+PA), the area under the tan-δ curve, specific toughness, and strain-at-break of the PHBV–HBP nanocomposite increased significantly for both solid and microcellular specimens, whereas the storage modulus, specific Young's modulus, and specific tensile strength decreased. The addition of 2% nanoclays into the PHBV–HBP nanocomposites improved the storage modulus, specific Young's modulus, and specific tensile strength of the PHBV–HBP–nanoclay-based nanocomposites, but they were still lower than those of the neat PHBV. POLYM. ENG. SCI., 51:1815–1826, 2011. © 2011 Society of Plastics Engineers

Correspondence to: Shaoqin Gong; e-mail: sgong@engr.wisc.edu

Contract grant sponsor: University of Wisconsin Solid Waste Research Program and National Science Foundation; contract grant number: CMMI 1032186.

DOI 10.1002/pen.21972

Published online in Wiley Online Library (wileyonlinelibrary.com).

INTRODUCTION

Broadening the use of biobased and biodegradable polymers such as poly(hydroxyalkanoates) (PHA) can reduce our dependence on petroleum-based polymers, which can have an adverse impact on the environment [1–3]. PHAs, a family of aliphatic polyesters, have drawn considerable attention in recent years due to their biodegradability and biocompatibility, natural origin, and close proximity in properties to some of the petroleum-based synthetic polymers [4–6].

Poly(hydroxybutyrate-*co*-hydroxyvalerate) (PHBV) is one of the most widely studied PHA polymer due to its potential use in a number of applications such as packaging, civil and construction, automotive, biomedical, and agricultural industries [7–10]. Nonetheless, currently, PHBV still has limited usage due to certain inferior mechanical properties (e.g., low elongation-at-break, low impact strength), poor thermal stability, and a narrow processing window ($\Delta T = 20^{\circ}$C), [11]. The toughness/impact strength of PHBV can be improved by blending with tough polymers [12–14], plasticizers [15, 16], and special additives such as hyperbranched polymers (HBPs) [17]. Blending PHBV with tough polymers is considered to be an effective approach to improve its toughness and elongation-at-break; however, it generally requires a relatively high amount of tough polymer and comes at the expense of a significant reduction in modulus and strength. The major shortcoming of using plasticizers is that these low molecular weight additives are inclined to migrate to the surface of the polymer components in long-term usage and, therefore, lead to brittleness [18]. Recent studies have shown that HBPs can effectively improve the impact strength of biobased polymers [19–22]. HBPs are dendritic, three-dimensional molecules with a repetitive branching

sequence and have a globular structure [21]. The unique characteristics, such as a high degree of branching, a broad molecular weight distribution, and a remarkably low viscosity (compared to linear polymers of similar molecular weights) allow HBPs to be used as compatibilizers and toughening agents for polymers and drug carriers in biomedical applications [23–28]. Inorganic nanofillers have been reported to improve the barrier properties, mechanical properties, and thermal stability of PHBV [29–32]. Many groups have reported that the incorporation of inorganic nanofillers led to a reduction in the thermal expansion coefficient and an enhancement in the Young's modulus, thermal stability, and heat deflection temperature as well as increased thermal stability [33, 34]. In this study, both inorganic nanofillers [i.e., Cloisite® 30B and Halloysite nanotubes (HNT)] and organic nanofillers (i.e., HBP) were incorporated into the PHBV matrix. Poly(maleic anhydride-*alt*-1-octadecene) (PA) was used as a crosslinking agent for HBP [19, 22]. The PHBV and PHBV-based nanocomposites (five formulations as listed in Table 1) were processed via both conventional and microcellular injection molding processes to produce solid and microcellular components, respectively. The effects of 12% (HBP+PA) and two different nanoclays (Cloisite 30B and HNT) on the mechanical, morphological, and thermal properties of the resulting PHBV–HBP–nanoclay-based nanocomposites were investigated.

For the microcellular injection molding process, supercritical fluid N_2 (SCF) was used as the physical foaming agent. There are three major steps involved in the microcellular injection molding process [35, 36]: (1) The SCF is injected into the polymer melt inside of the injection-molding barrel to form a single-phase polymer–gas solution; (2) A sudden pressure drop occurring at the nozzle or near the gate induces a thermodynamic instability in the polymer–gas solution, triggering cell nucleation; and (3) Cell growth continues in the mold, which is controlled by the gas diffusion rate and the stiffness of the polymer–gas solution. Microcellular components may be produced at a lower cost due to the use of less material and energy, and with a shorter cycle time [37–42]. Additionally, microcellular components also exhibit excellent dimensional stability [37–42]. For comparison purposes, solid components were also produced via the conventional injection molding process.

EXPERIMENTAL

Materials and Processing Conditions

PHBV was purchased, in pellet form, from Ningbo Tianan Biologic Material (Tianan-ENMAT; China) under the trade name Y1000P. It has a specific gravity of 1.24 and a melt flow index of 2.4 g/10 min at 170°C. The percentage of hydroxyvalerate in PHBV copolymer (Y1000P) is 2%. Hyperbranched polyester (HBP), under the trade name of Boltorn H2004® (molecular weight of 3100 g mol^{-1}), was provided by Perstorp Specialty Chemicals AB, Sweden. PA with a molecular weight of 30,000 to 50,000 g mol^{-1} was purchased from the Sigma-Aldrich Company. Halloysite® nanotubes (HNT) were also purchased from the Sigma-Aldrich Company. Halloysite ($Al_2Si_2O_5(OH)_4 \cdot 2H_2O$) has a multilayered aluminosilicate hollow tubular structure in the submicron range. The neighboring alumina and silica layers bend and form multilayer tubes due to the packing disorder. It has an average tube diameter of 50 nm, a typical specific surface area of 65 m^2 g^{-1}, and a specific gravity of 2.53 [43, 44]. Organically modified montmorillonite (MMT) nanoclay, Cloisite 30B, was obtained from Southern Clay Products. The MMT nanoclay was modified by an ion exchange reaction between the Na^+ present in the MMT nanoclay galleries and quaternary bis-(2-hydroxyethyl) methyl (hydrogenated tallowalkyl) ammonium cations.

The HBP, PA, Cloisite 30B, HNT, and processing aids (antioxidants and lubricant) were incorporated into the PHBV matrix in various formulations as shown in Table 1. The amount of (HBP+PA) used in the formulation was 12 wt%. PA was added to the formulations to improve further the toughness of the PHBV–HBP-based nanocomposites [19, 22]. A network between HBP and PA as the result of the reaction between the HBPs' hydroxyl groups, and the PA's anhydride groups was formed during the melt compounding process [25]. Based on the well-known reactivity of the HBP functional groups (six hydroxyl (—OH) functional groups), the required amount of anhydride group in PA was calculated. The molar ratio of hydroxyl (OH) to anhydride groups was set at 1:2, and it was calculated based on the numbers of hydroxyl and anhydride groups in HBP and PA, respectively [19]. The

TABLE 1. The formulations of PHBV and PHBV-based nanocomposites.

Formulation	PHBV (lb)	H2004 (lb)	PA (lb)	Cloisite® 30B (lb)	HNT (lb)	Naugard-10 (0.2%) (lb)	Naugard - 524 (0.2%) (lb)	Kemamide-W40 (0.1%) (lb)
PHBV	13.93	0.0	0.0	0.0	0.0	0.04	0.04	0.02
PHBV-12% HBP	17.5	1.6	0.8	0.0	0.0	0.04	0.04	0.02
PHBV-12% HBP-2% Cloisite 30B	17.1	1.6	0.8	0.4	0.0	0.04	0.04	0.02
PHBV-12% HBP-2% HNT	17.1	1.6	0.8	0.0	0.4	0.04	0.04	0.02
PHBV-12% HBP-1% HNT-1% Cloisite 30B	17.1	1.6	0.8	0.2	0.2	0.04	0.04	0.02

 DOI 10.1002/pen

amount of nanoclays (Cloisite 30B or HNT) used in the formulation was 2 wt%. For the PHBV–12% HBP–1% HNT–1% Cloisite 30B nanocomposite, the amount of HNT and Cloisite 30B used in the formulation was 1 wt% each. A kinetic mixer (K-mixer; Vanzetti Systems Series 3009) was used to prepare master batches (in quantities of 200 g) of PHBV, PA, Cloisite 30B, and HNT depending on the formulations. The K-mixer was turned on and once it reached around 150°C, it was turned off. After discharging, the molten blend was processed into a flat sheet and subsequently granulated. After mixing, the blends were dried at 80°C for 24 h. The liquid HBP used in the present study was incorporated into the master batches using a Cole–Parmer peristaltic pump (model #7553-80) and mixed in a twin-screw extruder. The corotating twin-screw extruder had a screw with a diameter of 32 mm and an L/D ratio of 36.25. Thereafter, mixed materials were injection molded using an Arberg Allrounder 320S (Lossburg, Germany) with a 25-mm diameter screw and equipped with Mucell® technology (Trexel, Woburn, MA). Solid and microcellular components were made. The processing conditions for conventional injection molding and microcellular injection molding are presented in Table 2.

The SCF weight percentage was calculated using *Eq. 1* [45].

$$\mathrm{SCF\,(wt\%)} = \frac{C\,\dot{m}\,t}{m} \tag{1}$$

where C is the conversion factor of 27.8, $\dot{m}$ is the mass flow rate of the SCF (kg h^{-1}), t is the SCF dosage time, and m is the shot weight (g).

Methods

Various techniques have been used to evaluate the mechanical, thermal, and morphological properties.

Tensile Testing

The tensile properties (modulus, strength, toughness, and elongation at break) were measured at room conditions using a 5 kN load cell on an Instron Model 5566 tensile tester. The extension was set at 25.4 mm min^{-1}. All tests were carried out according to the ASTM standard (ASTM-D638). Five specimens of each sample were tested, and the average results were reported.

Wide-Angle X-ray Diffraction

A wide-angle X-ray diffraction (WAXRD) analysis was performed using Scintag XDS 2000 with Ni-filtered Cu Ka radiation (0.15418 nm) at room temperature in the range of $2\theta = 1.5$–40° with a scanning rate of 2° min^{-1}.

Thermogravimetric Analysis

Thermogravimetric analysis (TGA) and derivative thermogravimetric analysis (DTG) tests were performed using a SDT 2960 thermogravimetric analyzer (TA Instruments) from 50 to 600°C with a heating ramp of 20°C min^{-1}under Argon flow (100 cm^3 min^{-1}).

Dynamic Mechanical Analysis

The dynamic mechanical analysis (DMA) experiments were carried out using a dynamic mechanical analyzer (DMA Q800; TA instruments). Rectangular specimens with a dimension of approximately 17.6 by 12.7 by 3.2 mm^3 were cut from injection molded parts and were tested in a single-cantilever mode. The heating rate was 3°C min^{-1} from –50 to 80°C with a frequency of 1 Hz and 0.02% prestrain, which is in the linear viscoelastic region as determined by a strain sweep.

Differential Scanning Calorimetry

Thermal properties were determined using differential scanning calorimetry (DSC; TA instruments; Auto DSC Q20). The weight of the DSC samples were between 7 and 9 mg. Samples were first heated from 40 to 200°C, kept isothermal for 3 min at 200°C, cooled down to –50°C, and then reheated to 200°C. The ramp rate for all heating and cooling cycles was 10°C min^{-1}. The crystallization temperature (T_c), melting temperature (T_m), apparent melting enthalpy (ΔH_f), and enthalpy of crystallization (ΔH_{cc}) were

TABLE 2. Injection molding processing parameters for PHBV and PHBV-based nanocomposites.

Samples		Mold temp. (°C)	Nozzle temp. (°C)	Pack pressure (MPa)	SCF dosage time (s)	Shot volume (cm^3)
PHBV	Solid	20	170	80	0	19.6
	Microcellular	20	190	0	0.3	19.6
PHBV-12% HBP	Solid	20	170	80	0	19.6
	Microcellular	20	190	0	0.1	17.0
PHBV-12% HBP-2% Cloisite 30B	Solid	20	170	80	0	19.8
	Microcellular	20	190	0	0.1	20.0
PHBV-12% HBP-2% HNT	Solid	20	170	80	0	19.6
	Microcellular	20	190	0	0.15	20.0
PHBV-12% HBP-1% HNT-1% Cloisite 30B	Solid	20	170	80	0	19.6
	Microcellular	20	190	0	0.15	20.0

determined from the DSC curves. T_m and ΔH_f were taken as the peak temperature and the area of the melting endotherm, respectively. The crystallinity (χ_c) of the PHBV phase was calculated by

$$\chi^c(\%\,\text{Crystallinity}) = \frac{\Delta H_f(\text{PHBV})}{\Delta H^\circ(\text{PHBV})} \times \frac{100}{w}. \quad (2)$$

where ΔH° (PHBV) is the enthalpy of melting per gram of 100% crystalline (perfect crystal) (109 J g^{-1}), and w is the weight fraction of PHBV in the blend [46].

To determine the crystallinity of the sample, the extra heat absorbed by the crystallites formed during heating (i.e., cold crystallization) had to be subtracted from the total endothermic heat flow due to the melting of the whole crystallites [47]. Thus, the modified equation can be written as follows:

$$\chi^c\,(\%\,\text{Crystallinity}) = \frac{\Delta H_f(\text{PHBV}) - \Delta H_{cc}(\text{PHBV})}{\Delta H^\circ(\text{PHBV})} \times \frac{100}{w}. \quad (3)$$

Scanning Electron Microscopy

Scanning electron microscopy (SEM) images of the fracture surfaces of injection-molded specimens were obtained using an ultra-high resolution FE-SEM (Hitachi S-4800) operated at 5 kV. The fracture surfaces were obtained by freeze-cracking the injection-molded samples using liquid N_2. All specimens were sputter coated with a thin layer of gold–palladium (5 nm) before examination. The comparison between the SEM images of different specimens was made at the same magnification.

Analysis of the average cell size and cell density was performed quantitatively using an image analysis tool (UTHSCSA image tool). The cell density was calculated using the following formula [48]:

$$\text{Cell Density} = \left(\frac{N}{L^2}\right)^{1.5} \times M \quad (4)$$

where N is the number of cells, L is the linear length of the area, and M is a unit conversion resulting in the number of cells per cm^3.

Transmission Electron Microscopy

The structure of the PHBV–HBP–nanoclay-based nanocomposites polymer was investigated using a Hitachi H-600 transmission electron microscopy (TEM) operated at 75 kV. The ultrathin sections with a thickness of 70 nm were prepared at room temperature (~25°C) using an RMC ultramicrotome (Model# MT-7000) without staining. The TEM sections were taken from the middle portion of the tensile test specimens.

RESULTS AND DISCUSSION

Microstructure Analysis via WAXRD and TEM

The structure of solid and microcellular PHBV–HBP–nanoclay-based nanocomposites were studied using WAXRD and TEM as shown in Figs. 1 and 2, respectively. The interlayer distance of the nanoclays (Cloisite 30B and HNT) was calculated based on the Bragg's equation $\lambda = 2d \sin\theta$ (wavelength (λ) of the X-ray was 0.154 nm) [49].

As can be seen in Fig. 1A and B, the WAXRD patterns revealed the (001) diffraction peaks at ($2\theta = 5.08^\circ$ for Cloisite 30B and $2\theta = 12.24^\circ$ for HNT) with an interlayer spacing (d_{001}= 1.73 nm for Cloisite 30B and 0.72 nm for HNT). For the solid and microcellular PHBV–12% HBP–2% Cloisite 30B nanocomposites (Fig. 1C and D, respectively), the diffraction peaks of the Cloisite 30B disappeared. Qualitative analysis of the TEM images of the solid and microcellular PHBV–12% HBP–2% Cloisite 30B nanocomposites (Fig. 2A and B, respectively) showed a combination of exfoliation and heterogeneous intercalation of Cloisite 30B was observed for both solid and microcellular PHBV–12% HBP–2% Cloisite 30B nanocomposites [50, 51]. According to Chen et al. [52], heterogeneous intercalation accompanied with nonuniform interlayer distances might lead to the disappearance of the nanoclay's diffraction peak. For the PHBV–12% HBP–2% HNT nanocomposite, the (001) diffraction peak of the HNT (indicated with black arrows) was observed at $2\theta = 12.24^\circ$ for the solid components (Fig. 1E) and $2\theta = 12.22^\circ$ for the microcellular components (Fig. 1F) (i.e., d_{001} = 0.72 nm for both solid and microcellular components) in the diffraction pattern indicating the interlayer spacing of the HNT was unchanged after being incorporated into the PHBV matrix [53–56]. TEM images (Fig. 2C and D)

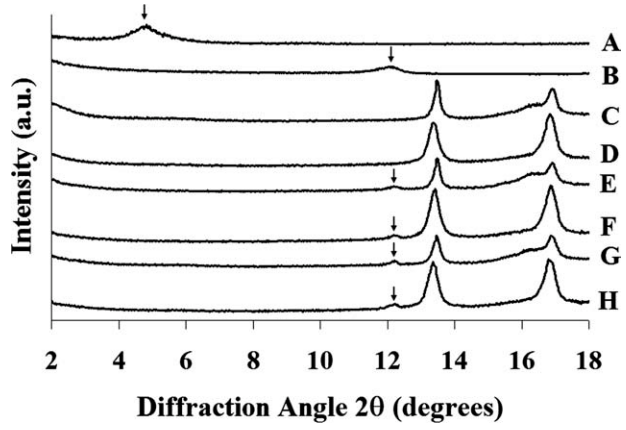

FIG. 1. Wide-angle XRD patterns of (A) Cloisite® 30B, (B) HNT, (C) PHBV–12% HBP–2% Cloisite 30B (solid), (D) PHBV–12% HBP–2% Cloisite 30B (microcellular), (E) PHBV–12% HBP–2% HNT (solid), (F) PHBV–12% HBP–2% HNT (microcellular), (G) PHBV–12% HBP–1% HNT–1% Cloisite 30B (solid), and (H) PHBV–12% HBP–1% HNT–1% Cloisite 30B (microcellular).

DOI 10.1002/pen

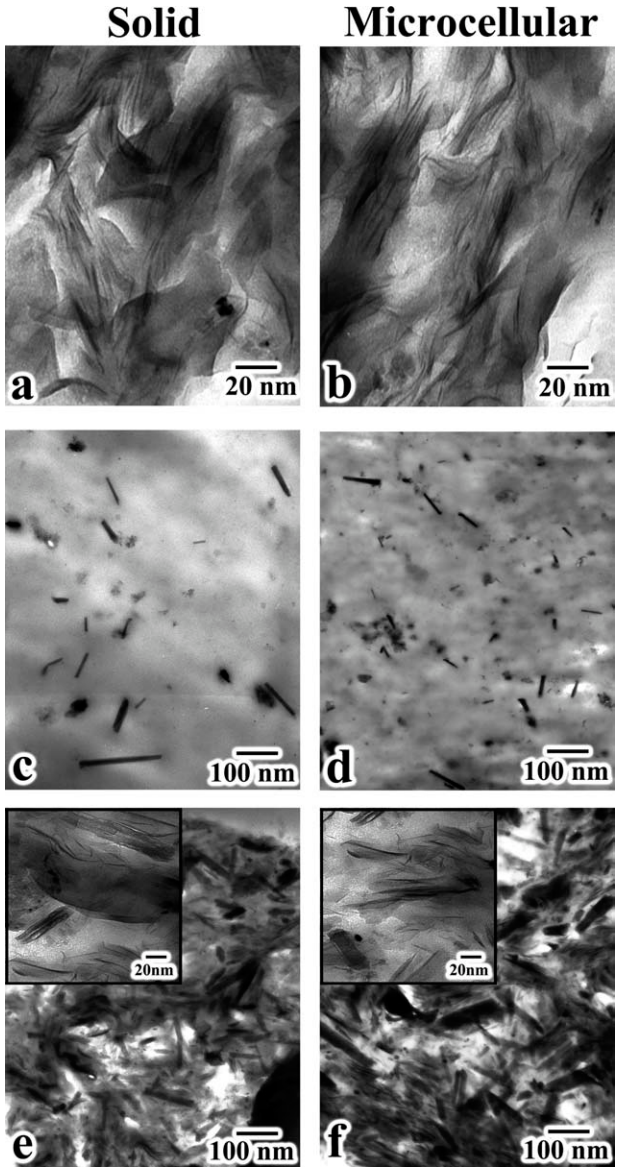

FIG. 2. TEM images of (a, b) PHBV–12% HBP–2% Cloisite® 30B, (c, d) PHBV–12% HBP–2% HNT, and (e, f) PHBV–12% HBP–1% HNT–1% Cloisite 30B.

showed that HNTs were dispersed individually and uniformly within the PHBV matrix for both the solid and microcellular PHBV–HBP–HNT nanocomposite. A similar observation was reported in other studies related to HNTs [56–58]. For the solid and microcellular PHBV–12% HBP–1% HNT–1% Cloisite 30B nanocomposites (Fig. 1G and H), the diffraction peak of Cloisite 30B for both solid and microcellular components disappeared. Combined with the TEM images of the solid and microcellular PHBV–12% HBP–1% HNT–1% Cloisite 30B nanocomposites shown in Fig. 2E and F, respectively, a combination of exfoliation and heterogeneous intercalation for Cloisite 30B was observed for both solid and microcellular PHBV–12% HBP–1% HNT–1% Cloisite 30B nanocomposites [50–52]. The diffraction peak of HNT (indicated with black arrows) again appeared at $2\theta = 12.24^\circ$ for the solid components and at $2\theta = 12.22^\circ$ for the microcellular components indicating a constant interlayer spacing before or after being incorporated into the PHBV matrix.

Morphology of the Fractured Surfaces of Both Solid and Microcellular Components

Figure 3 shows the SEM images of the PHBV and PHBV-based nanocomposites. Both solid and microcellular samples were investigated. As can be seen from the images shown in Fig. 3a, the tensile fractured surfaces of the solid PHBV components were relatively smooth, indicating that the samples fractured under the brittle mode. This observation was supported by the values of specific

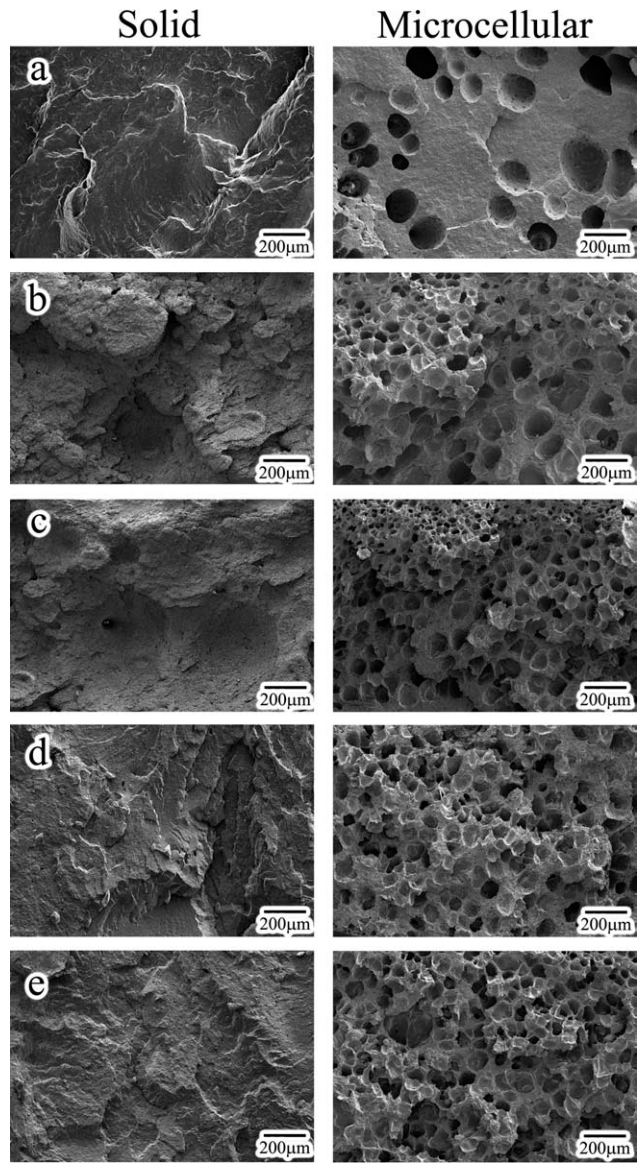

FIG. 3. Tensile fractured surfaces of the solid and microcellular components made of (a) PHBV, (b) PHBV–12% HBP, (c) PHBV–12% HBP–2% Cloisite® 30B, (d) PHBV–12% HBP–2% HNT, and (e) PHBV–12% HBP–1% HNT–1% Cloisite 30B.

toughness and strain-at-break obtained from the tensile tests. For all solid PHBV-based nanocomposites (Fig. 3b–e), their tensile-fractured surfaces had a relatively higher roughness, indicating a high degree of plastic deformation.

Figure 3a–e show the representative images of the tensile-fractured surface of the microcellular PHBV and PHBV-based nanocomposites. A quantitative analysis of the average cell size and cell density was performed using an image analysis tool (UTHSCSA Image Tool), and the results are summarized in Table 3. Quantification of the cellular structure was done on the center portion of the tensile bar cross sections. Variations in cell size and cell density occurred throughout the thickness of the part due to shear and rapid cooling at the polymer-mold interface.

As shown in Table 3, with the addition of 12% (HBP+PA), the cell size of the microcellular PHBV–HBP nanocomposite decreased by half and the cell density increased by approximately one order of magnitude. Adding 2% Cloisite 30B, 2% HNT, or 1% Cloisite 30B–1% HNT further decreased the cell size and increased the cell density. The reduction in cell size and increment in cell density observed with the addition of (HBP+PA), Cloisite 30B, and HNT can be attributed to a couple of factors: (1) Nanofillers such as (HBP+PA), Cloisite 30B and HNT acted as nucleating agents, thereby, leading to more uniform cell nucleation and growth [59]; and (2) The addition of nanofillers may have increased the melt viscosity and induced strain hardening, which could limit the cell growth and coalescence [60].

Thermal Properties

Thermal Decomposition Behavior. The thermal stability of the PHBV and PHBV-based nanocomposites were studied using TGA. Figure 4a and b show the weight loss curves of the PHBV and PHBV-based nanocomposites. Figure 4b is a magnified version of Fig. 4a in the major weight loss area (250–310°C). As can be seen from the TGA curves, one major weight loss step was observed in all samples, which is attributed to thermal degradation of PHBV [61].

The difference in thermal decomposition behavior of the samples can be distinguished more obviously from the derivative thermogravimetry (DTG) curves shown in Fig. 4c (i.e., the derivatives of weight loss with respect to time [dw/dt (min)]). The DTG curve exhibited a single peak for all samples indicating thermal degradation consisted of one major weight loss step. The onset tempera-

TABLE 3. Representative values of the average cell size and cell density of the microcellular PHBV and PHBV-based nanocomposites.

Samples	Avgerage cell size (μm)	Cell density (Number/cm^3)
PHBV	120 ± 41	2.31 E + 05
PHBV-12% HBP	59 ± 24	2.50 E + 06
PHBV-12% HBP-2% Cloisite 30B	51 ± 14	2.87 E + 06
PHBV-12% HBP-2% HNT	55 ± 23	2.63 E + 06
PHBV-12% HBP-1% HNT-1% Cloisite 30B	52 ± 19	2.76 E + 06

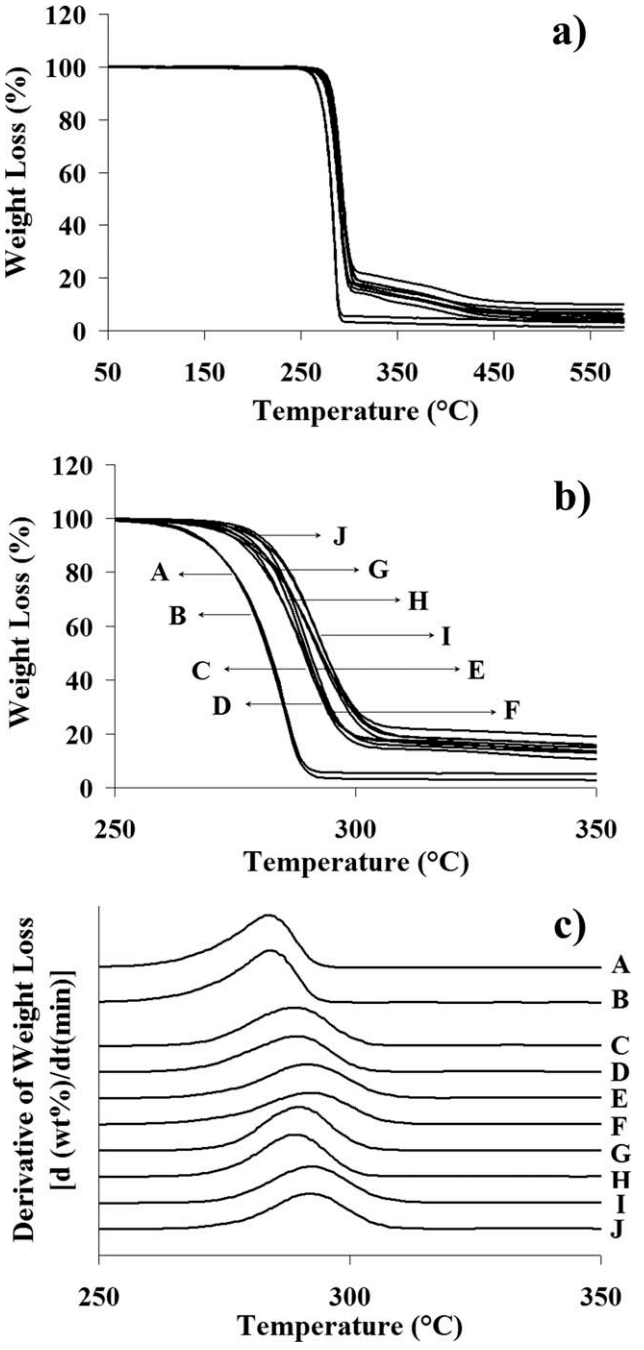

FIG. 4. (a) and (b) weight loss of PHBV and PHBV-based nanocomposites with temperature, and (c) derivative of the weight loss as a function of temperature: (A) PHBV (solid); (B) PHBV (microcellular); (C)PHBV–12% HBP (solid); (D) PHBV–12% HBP (microcellular); (E) PHBV–12% HBP–2% Cloisite® 30B (solid); (F) PHBV–12% HBP–2% Cloisite 30B (microcellular); (G) PHBV–12% HBP–2% HNT (solid); (H) PHBV–12% HBP–2% HNT (microcellular); (I) PHBV–12% HBP–1% HNT–1% Cloisite 30B (solid); and (J) PHBV–12% HBP–1% HNT–1% Cloisite 30B (microcellular).

DOI 10.1002/pen

TABLE 4. The onset degradation temperatures, the derivative thermogravimetry peak temperatures, and the ash contents of the PHBV and PHBV-based nanocomposites.

Samples		Onset degradation temperature (°C)	DTG peak temperature (°C)	Ash content (%)
PHBV	Solid	282.0	284.2	1.4
	Microcellular	282.4	284.6	3.6
PHBV-12% HBP	Solid	289.4	288.9	3.8
	Microcellular	289.5	289.5	6.1
PHBV-12% HBP-2% Cloisite 30B	Solid	292.8	291.7	4.5
	Microcellular	293.1	292.0	6.7
PHBV-12% HBP-2% HNT	Solid	290.1	292.1	5.2
	Microcellular	290.9	292.2	7.9
PHBV-12% HBP-1% HNT-1% Cloisite 30B	Solid	293.8	293.3	6.3
	Microcellular	293.8	293.4	10.0

ture (i.e., the temperature at which 50% degradation occurs) and the peak temperatures of the DTG curves (i.e., the mid-points of the degradation steps) are measures of thermal stability [61–63].

The onset degradation temperatures, the peak temperatures obtained by DTG, and the ash content are listed in Table 4. The addition of 12% (HBP+PA) increased the onset degradation temperature and DTG peak temperature for both solid and microcellular components compared to the neat PHBV, which can be attributed to the higher thermal stability of 12% (HBP+PA) (decomposition temperature 300°C) [21]. The addition of 2% Cloisite 30B, 2% HNT, or 1% HNT–1% Cloisite 30B further increased the onset degradation temperature and DTG peak temperature for both solid and microcellular components.

The enhanced thermal stability observed in the three PHBV-nanoclay based nanocomposites can be attributed to the fact that nanoclays act as heat barriers and thus retard the thermal degradation of the composites [64]. Furthermore, as can be seen in Table 4, with the addition of (HBP+PA), Cloisite 30B and HNT, the ash content increased compared to neat PHBV for both solid and microcellular components due to increased thermal stability [21, 64]. Also, for the same formulation, the microcellular components had higher ash content compared to their solid counterparts, which might be due to the lower thermal conductivity, and, thus, better thermal insulation property exhibited by the microcellular components [65].

Crystallinity and Melting Behavior. Thermal properties (crystallization and melting behavior) of PHBV and PHBV-based nanocomposites were studied using DSC. The thermograms and the numerical values of melting temperatures, enthalpy of meltings, and the degrees of crystallinities obtained from the second heating cycle are presented in Fig. 5 and Table 5, respectively. The thermograms and data obtained from the second heating cycle provide information on the crystallization and melting behavior of the samples without the influence of different thermal histories.

As can be seen in Fig. 5, for both the solid and microcellular components, unlike the neat PHBV, which showed a single melting peak, all PHBV-based nanocomposites exhibited double melting peaks. This may be attributed to different types of crystalline structures or a variation in thickness of the lamellar structure and size of the spherulites obtained during the crystallization process of the composites [66–69].

Table 5 shows the degree of crystallinity (χ) of PHBV in the filled composites for solid and microcellular components obtained from the second heating cycle. With the addition of 12% 12% (HBP+PA), the degree of crystallinity increased by approximately 3% for both solid and microcellular components. This may be attributed to the fact that 12% (HBP+PA) enhanced the free volume of PHBV chains, which subsequently improved the chains' mobility and, therefore, the crystallization increased [19]. Also, the addition of 2% Cloisite 30B, 2% HNT, or 1% HNT–1% Cloisite 30B further increased the degree of crystallinity of the PHBV–HBP–nanoclay-based nano-

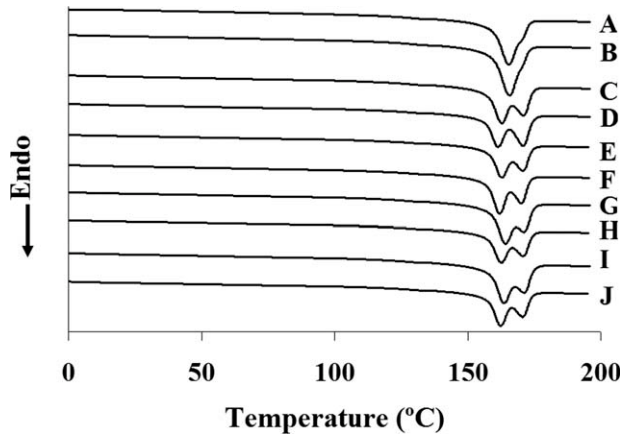

FIG. 5. Thermograms of solid and microcellular PHBV and PHBV-based nanocomposites obtained from the second heating run: (A) PHBV (solid), (B) PHBV (microcellular), (C) PHBV–12% HBP (solid), (D) PHBV–12% HBP (microcellular), (E) PHBV–12% HBP–2% Cloisite® 30B (solid), (F) PHBV–12% HBP–2% Cloisite 30B (microcellular), (G) PHBV–12% HBP–2% HNT (solid), (H) PHBV–12% HBP–2% HNT (microcellular), (I) PHBV–12% HBP–1% HNT–1% Cloisite 30B (solid), and (J) PHBV–12% HBP–1% HNT–1% Cloisite 30B (microcellular).

TABLE 5. Thermal characteristics of the solid and microcellular PHBV and PHBV-based nanocomposites obtained from the second heating run.

Samples		Melting (second heating) Temperature (°C)		Crystallinity (%)	Enthalpy (J g^{-1})
Solid	PHBV	165.6		70.1	64.3
	PHBV-12% HBP	162.9	171.1	64.7	67.4
	PHBV-12% HBP-2% Cloisite 30B	162.9	170.8	66.8	71.3
	PHBV-12% HBP-2% HNT	164.2	170.1	64.3	68.5
	PHBV-12% HBP-1% HNT-1% Cloisite 30B	163.8	171.1	63.7	68.0
Microcellular	PHBV	165.8		69.4	63.7
	PHBV-12% HBP	161.4	172.9	64.3	67.0
	PHBV-12% HBP-2% Cloisite 30B	162.1	173.4	66.6	71.1
	PHBV-12% HBP-2% HNT	162.7	172.9	64.4	68.7
	PHBV-12% HBP-1% HNT-1% Cloisite 30B	162.5	173.7	62.2	67.9

composites, likely due to the fact that the nanoclays acted as crystallization nucleating agents [66, 70, 71]. For the same formulation, there is no significant difference in the degree of the crystallinity of the solid and microcellular components.

Mechanical Properties

Weight Reduction of the Microcellular Components. The weight reductions of the microcellular components were 13.0, 11.2, 11.1, 10.2, and 9.7 for PHBV, PHBV–12% HBP nanocomposite, PHBV–12% HBP–2% Cloisite 30B nanocomposite, PHBV–12% HBP–2% HNT nanocomposite, and PHBV–12% HBP–1% HNT–1% Cloisite 30B nanocomposite, respectively.

Dynamic Mechanical Properties. DMA was used to study the viscoelastic properties of the solid and microcellular PHBV and PHBV-based nanocomposites. It should be mentioned that the dynamic mechanical properties of solid and microcellular components in this study are reported without taking the weight reduction of microcellular samples into consideration. The effect of temperature on the storage modulus of different samples is depicted in Fig. 6a. In the glassy region (<20°C), the storage modulus of solid and microcellular components decreased with the addition of 12% (HBP+PA). This might be attributed to the free volume enhancement of the PHBV chains as a result of the 12% (HBP+PA) addition [25]. Addition of 2% Cloisite 30B, 2% HNT, or 1% HNT–1% Cloisite 30B increased the storage modulus of solid and microcellular components

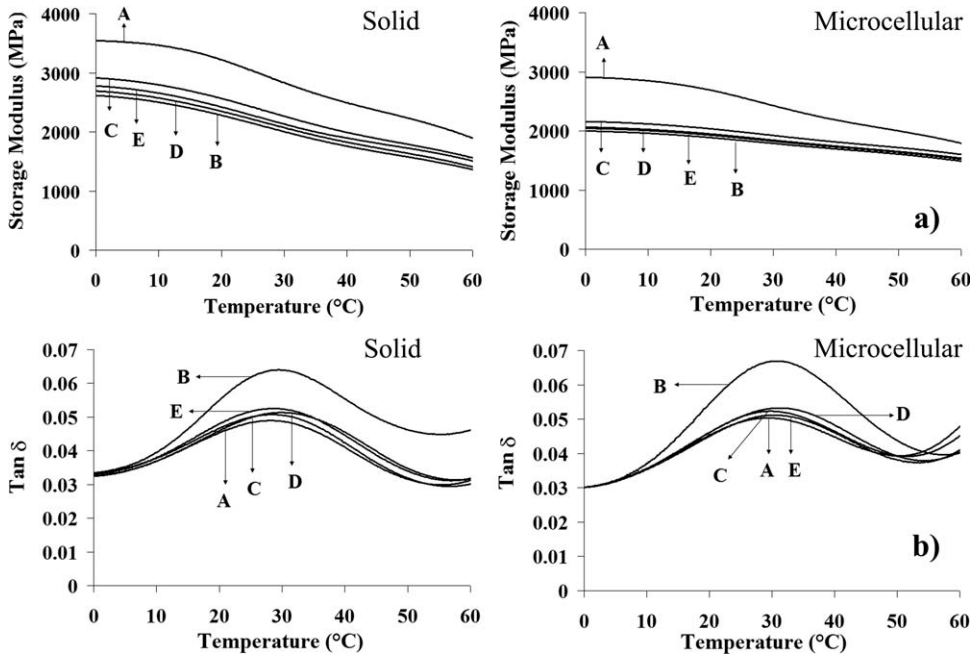

FIG. 6. Viscoelastic properties of the solid and microcellular PHBV and PHBV-based nanocomposites: (a) Storage modulus as a function of temperature; (b) Loss factor (Tan-δ) as a function of temperature: (A) PHBV; (B) PHBV–12% HBP; (C) PHBV–12% HBP–2% Cloisite 30B; (D) PHBV–12% HBP–2% HNT; (E) PHBV–12% HBP–1% HNT–1% Cloisite 30B.

 DOI 10.1002/pen

compared to PHBV–HBP nanocomposite, which might be due to the restriction of the PHBV chains' segmental motions as a result of the addition of Cloisite 30B and HNT and their subsequent exfoliation and heterogeneous intercalation [72]; however, their storage moduli were still lower than that of neat PHBV. For the same formulation, solid components had higher values of storage modulus in comparison to their microcellular counterparts, which might be attributed to the presence of certain large voids in the microcellular components as a result of the dynamic nature of the microcellular injection molding process [39].

Figure 6b and Table 6 show the Tan-δ curves and the numerical values of T_g and the area underneath the Tan-δ peak of all of the samples. The area underneath the Tan-δ peak represents the damping ability of the material; that is, the material's ability to absorb and dissipate energy [68]. As can be seen in Fig. 6b and Table 6, the area underneath the Tan-δ peak of the solid components increased with the addition of 12% (HBP+PA) compared with that of the pure PHBV indicating that the PHBV–HBP nanocomposite had better damping ability than neat PHBV. The addition of 2% Cloisite 30B, 2% HNT, or 1% HNT–1% Cloisite 30B caused a decrease in the area underneath the Tan-δ peak for both solid and microcellular components compared to that of the PHBV–HBP nanocomposite. However, the areas underneath the Tan-δ peak for the three PHBV–HBP–nanoclay-based nanocomposites were similar to that of neat PHBV for both solid and microcellular components. In addition, the glass transition temperatures of the PHBV–HBP–nanoclay-based nanocomposites were all similar to that of PHBV.

Static Mechanical Properties

Figure 7 shows the results of the tensile tests (according to ASTM-D638) performed on the injection-molded solid and microcellular components of the PHBV and PHBV-based nanocomposites. Properties such as specific modulus, energy-to-break (specific toughness), strain-at-break, and specific strength were measured. Specific properties (i.e., specific strength, modulus, and toughness) were obtained by taking into account the density reduction.

As shown in Fig. 7a, the addition of 12% (HBP+PA) enhanced the specific toughness by 85 and 87% for the solid and microcellular components, respectively. The increase in toughness suggests that the dispersed 12% (HBP+PA) particles behaved as rubber particles and might have promoted multiple crazing, shear yielding, and cavitation [19, 73–75]. Adding 2% Cloisite 30B, 2% HNT, or 1% HNT–1% Cloisite 30B to the PHBV–HBP nanocomposites resulted in a decrement in specific toughness for both solid and microcellular PHBV–HBP–nanoclay-based nanocomposite components, which might be attributed to poor interfacial properties between the nanoclay and PHBV matrix [76]; however, their specific toughnesses were still higher than that of neat PHBV. These results are in agreement with the data obtained from the DMA (i.e., the area under the Tan-δ curve).

Among the three different nanoclay formulations, the PHBV–12% HBP–1% HNT–1% Cloisite 30B nanocomposite had the lowest toughness, which might be due to the aggregation of HNTs that acted as stress concentration spots and resulted in a decrement in toughness [72]. Also, compared with their solid counterparts, microcellular components had higher average specific toughness values, which may be attributed to the smaller cell sizes and higher cell densities observed in the microcellular components. These microcells act as crack arrestors, thereby improving the specific toughness [37, 38, 77].

A similar trend was observed for the strain-at-break of PHBV and PHBV-based nanocomposites (Fig. 7b). With the addition of 12% (HBP+PA), the strain-at-break increased significantly, by 67 and 152% for solid and microcellular components, respectively, compared to that of neat PHBV. With the addition of 2% Cloisite 30B, 2% HNT, or 1% HNT–1% Cloisite 30B, the strain-at-break of the resulting PHBV–HBP–nanoclay-based nanocomposites decreased for both solid and microcellular components compared to that of the PHBV–HBP nanocomposite. However, their strain-at-break was still higher than that of neat PHBV.

As shown in Fig. 7c, with the addition of 12% (HBP+PA), the specific tensile strength decreased for both solid and microcellular components compared to

TABLE 6. Numeric data of the glass transition temperature and the area underneath the Tan-**δ** peak of the solid and microcellular PHBV and PHBV-based nanocomposites.

Samples		Area under the tan-δ curve (°C)	T_α (°C)
PHBV	Solid	2.2	28.3
	Microcellular	2.3	29.5
PHBV-12% HBP	Solid	2.8	30.5
	Microcellular	3.2	30.8
PHBV-12% HBP-2% Cloisite 30B	Solid	2.3	28.5
	Microcellular	2.4	30.4
PHBV-12% HBP-2% HNT	Solid	2.4	28.4
	Microcellular	2.4	29.7
PHBV-12% HBP-1% HNT-1% Cloisite 30B	Solid	2.3	30.0
	Microcellular	2.4	30.3

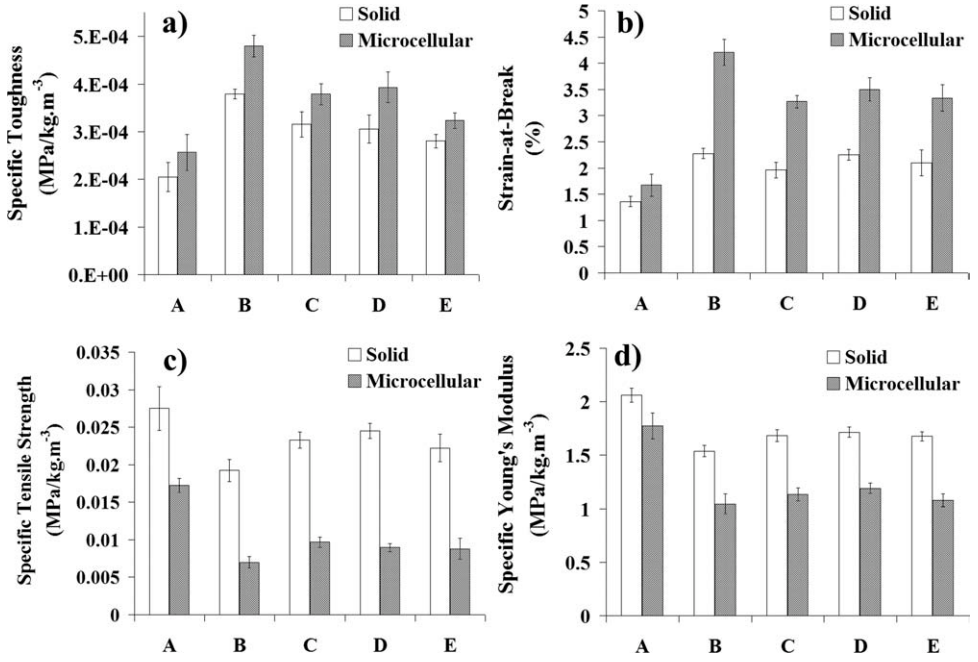

FIG. 7. Specific mechanical properties of solid and microcellular PHBV and PHBV-based nanocomposites: (a) Specific toughness (MPa/kg m^{-3}); (b) Strain-at-break (%); (c) Specific tensile strength (MPa/kg·m^{-3}); (d) Specific Young's modulus (MPa/kg m^{-3}): (A) PHBV; (B) PHBV–12% HBP; (C) PHBV–12% HBP–2% Cloisite® 30B; (D) PHBV–12% HBP–2% HNT; and (E) PHBV–12% HBP–1% HNT–1% Cloisite 30B.

neat PHBV. It is common to observe a reduction in tensile strength and modulus in toughened polymer composites [22]. In this study, the reduction in tensile strength was 30% for the solid components and 58% for the microcellular components. With the addition of 2% Cloisite 30B, 2% HNT, or 1% HNT–1% Cloisite 30B, the specific tensile strength of the resulting PHBV–HBP–nanoclay-based nanocomposites increased compared to that of the PHBV–HBP nanocomposite for both solid and microcellular components, which may be attributed to the uniform dispersion of HNT and the exfoliation and heterogeneous intercalation of Cloisite 30B in the PHBV–HBP–nanoclay-based nanocomposites [72, 78, 79]. Also, for the same formulation, microcellular samples had lower specific tensile strengths compared to their solid counterparts, which might be due to the presence of certain large cells in the microcellular samples acting as stress concentrators [80].

As shown in Fig. 7d, with the addition of 12% (HBP+PA), the specific Young's modulus decreased for both solid and microcellular components compared to neat PHBV. However, with further addition of 2% Cloisite 30B, 2% HNT, or 1% HNT–1% Cloisite 30B, the specific Young's modulus of the resulting PHBV–HBP–nanoclay-based nanocomposites increased. This may also be attributed to the uniform dispersion of HNT and the exfoliation and heterogeneous intercalation of Cloisite 30B in these PHBV–HBP–nanoclay-based nanocomposites, as discussed in the previous section [72, 78, 79]. In addition, there was no significant variation in the specific Young's modulus of the PHBV–HBP–nanoclay-based nanocomposites. Moreover, microcellular samples had lower tensile Young's moduli compared to their solid counterparts in the same formulation, which might be due to the presence of certain large microcells, which acted as stress concentrators [80].

CONCLUSIONS

Solid and microcellular PHBV and PHBV-based nanocomposites were processed using both conventional and microcellular injection molding processes. Five different formulations have been processed including (1) PHBV, (2) PHBV–12% (HBP+PA) nanocomposite, (3) PHBV–12% (HBP+PA)–2% Cloisite 30B nanocomposite, (4) PHBV–12% (HBP+PA)–2% HNT nanocomposite, and (5) PHBV–12% (HBP+PA)–1% HNT–1% Cloisite 30B nanocomposite. According to WAXRD and TEM analyses, Cloisite 30B was observed to exhibit a combination of exfoliation and heterogeneous intercalation structure in the PHBV–HBP–nanoclay-based nanocomposites. Also, the (001) interlayer spacing of HNT did not change before or after being incorporated into the PHBV matrix and TEM analysis showed that HNT dispersed uniformly in the PHBV matrix. The addition of 2% Cloisite 30B, 2% HNT, or 1% HNT–1% Cloisite 30B into the PHBV matrix improved the thermal stability of the PHBV–HBP–nanoclay-based nanocomposites. The addition of (HBP+PA), Cloisite 30B, and HNT reduced the average cell size and increased the cell density of the microcellular components. The degree of

crystallinity increased with the incorporation of (HBP+PA), Cloisite 30B, and HNT for both solid and microcellular components. The addition of 12% (HBP+PA) decreased the storage modulus of the PHBV–HBP nanocomposite for both solid and microcellular components. However, the addition of 2% Cloisite 30B, 2% HNT, or 1% HNT–1% Cloisite 30B into the PHBV–HBP nanocomposite increased the storage modulus of the resulting PHBV–HBP–nanoclay-based nanocomposites for both solid and microcellular components; however, they were still lower than that of neat PHBV. The addition of 12% (HBP+PA) into PHBV increased the specific toughness and strain-at-break significantly for both solid and microcellular components; however, the addition of 2% Cloisite 30B, 2% HNT, or 1% HNT–1% Cloisite 30B into the PHBV–HBP nanocomposite decreased the specific toughness and strain-at-break of the PHBV–HBP–nanoclay-based nanocomposites. On the other hand, the specific tensile strength and specific Young's modulus were reduced with the incorporation of 12% (HBP+PA) for both solid and microcellular components; however, with further addition of 2% Cloisite 30B, 2% HNT, or 1% HNT–1% Cloisite 30B, the specific tensile strength and specific Young's modulus of the resulting PHBV–HBP–nanoclay-based nanocomposites were improved slightly compared to the PHBV–HBP nanocomposite.

REFERENCES

1. S. Philip, T. Keshavarz, and I. Roy, *J. Chem. Technol. Biotechnol.*, **82**, 233 (2007).
2. M. Avella, G.B. Gaceva, A. Buzarovska, M.E. Errico, and G. Gentile, *J. Appl. Polym. Sci.*, **104**, 3192 (2007).
3. K.G. Satyanarayana, G.G.C. Arizaga, and F. Wypych, *Prog. Polym. Sci.*, **34**, 982 (2009).
4. A.K. Mohanty, M. Misra, and L.T. Drzal, *J. Polym. Environ.*, **10**, 19 (2002).
5. K. Sudesh, H. Abe, and Y. Doi, *Prog. Polym. Sci.*, **25**, 1503 (2000).
6. N.M. Barkoulaa, S.K. Garkhaila, and T. Peijs, *Ind. Crop. Prod.*, **31**, 34 (2010).
7. G. Adamus, *Macromol. Symp.*, **239**, 77 (2006).
8. G.G.Q. Chen, *Biodegradable Polymers for Industrial Applications*, CRC Press Ltd, Cambridge (2005).
9. I. Gursel, C. Balcik, Y. Arica, O. Akkus, N. Akkas, and V. Hasirci, *Biomaterials*, **19**, 1137 (1998).
10. J. Xu and D. Pierick, *J Inject. Mold. Technol.*, **5**, 152 (2001).
11. B. Fei, C. Chen, H. Wu, S. Peng, X. Wang, L. Dong, and J.H. Xin, *Polymer*, **45**, 6275 (2004).
12. A. Marcilla, J.C. Garcia-Quesada, and E. Gil, *J. Appl. Polym. Sci.*, **110**, 2102 (2008).
13. J. Li, M.F. Lai, and J.J. Liu *J. Appl. Polym. Sci.*, **98**, 1427 (2005).
14. E.S. Park, H.K. Kim, J.H. Shim, H.S. Kim, L.W. Jang, and J.S. Yoon, *J. Appl. Polym. Sci.*, **92**, 3508 (2004).
15. G. Ceccoruli, M. Pizzoli, and M. Scandola, *Macromolecules*, **26**, 6722 (1993).
16. B.J. Tighe, A.J. Amass, and M. Yasin, *Macromol. Symp.*, **123**, 133 (1997).
17. A.K. Mohanty and R. Bhardwaj, U.S. Patent 7,579,413 (2009).
18. Y. Lin, K.Y. Zhang, Z.M. Dong, L.S. Dong, and Y.S. Li, *Macromolecules*, **40**, 6257 (2007).
19. R. Bhardwaj and A.K. Mohanty, *Biomacromolecules*, **8**, 2476 (2007).
20. C. Gao and D. Yan, *Prog. Polym. Sci.*, **29**, 183 (2004).
21. J.F. Zhang and X. Sun, *Polym. Int.*, **53**, 716 (2004).
22. S. Pilla, A. Kramschuster, J. Lee, C. Clemons, S. Gong, and L.S. Turng, *J. Mater. Sci.*, **45**, 2732 (2010).
23. Y. Hong, S.J. Coombs, J.J. Cooper-White, M.E. Mackay, C.J. Hawker, E. Malmstrom, and N. Rehnberg, *Polymer*, **41**, 7705 (2000).
24. G. Jannerfeldt, L. Boogh, and J.A.E. Manson, *Polymer*, **41**, 7627 (2000).
25. S.B. Kil, Y. Augros, Y. Leterrier, and J.A.E. Manson, *Polym. Eng. Sci.*, **43**, 329 (2003).
26. M. Prabaharan, J.J. Grailer, S. Pilla, D.A. Steeber, and S. Gong, *Macromol. Biosci.*, **9**, 515 (2009).
27. M. Prabaharan, J.J. Grailer, S. Pilla, D.A. Steeber, and S. Gong, *Biomaterials*, **30**, 3009 (2009).
28. R. Mezzenga, L. Boogh, and J.A.E. Manson, *Compos. Sci. Technol.*, **61**, 787 (2001).
29. W.M. Choi, T.W. Kim, O.O. Park, Y.K. Chang, and J.W. Lee, *J. Appl. Polym. Sci.*, **90**, 525 (2003).
30. S. Wang, C. Song, G. Chen, T. Guo, J. Liu, and B. Zhang, *Polym. Degrad. Stabil.*, **87**, 69 (2005).
31. G.X. Chen, G.J. Hao, T.Y. Guo, M.D. Song, and B.H. Zhang, *J. Appl. Polym. Sci.*, **93**, 655 (2004).
32. G.X. Chen, G.J. Hao, T.Y. Guo, M.D. Song, and B.H. Zhang, *J. Mater. Sci. Lett.*, **21**, 1587 (2002).
33. V.N. Hristov and S.T. Vasileva, *Polym. Compos.*, **25**, 521 (2004).
34. Y. Zhong, T. Poloso, M. Hetzer, and D.D. Kee, *Polym. Eng. Sci.*, **47**, 797 (2007).
35. S. Gong, L.S. Turng, C. Park, and L. Liao, *Microcellular Polymer Nanocomposites for Packaging and other Applications*, American Scientific Publishers, Chapter 6, p 144 (2008).
36. S. Gong, M. Yuan, A. Chandra, A. Winardi, A. Osorio, and L.S. Turng, *Int. Polym. Process.*, **2**, 202 (2005).
37. S. Pilla, S. Gong, E. O'Neill, R.M. Rowell, and A.M. Krzysik, *Polym. Eng. Sci.*, **48**, 578 (2008).
38. S. Pilla, A. Kramschuster, S. Gong, A. Chandra, and L.S. Turng, *Int. Polym. Process.*, **22**, 418 (2007).
39. S. Pilla, L. Yang, S. Gong, E. O'Neill, and R.M. Rowell, *J. Appl. Polym. Sci.*, **111**, 37 (2009).
40. A. Javadi, Y. Srithep, S. Pilla, J. Lee, C. Clemons, S. Gong, and L.S. Turng, *Compos. Part A: Appl. Sci.*, **41**, 982 (2010).
41. A. Javadi, Y. Srithep, S. Pilla, J. Lee, S. Gong, and L.S. Turng, *Mater. Sci. Eng. C.*, **30**, 749 (2010).
42. A. Javadi, A.J. Kramschuster, S. Pilla, J. Lee, S. Gong, and L.S. Turng, *Polym. Eng. Sci.*, **50**, 1440 (2010).
43. E. Joussein, S. Petit, and J. Churchman, *Clay Miner.*, **40**, 383 (2005).

44. E. Hope and J. Kittrick, *Am. Mineral*., **49**, 859 (1964).
45. A. Kramschuster, S. Pilla, S. Gong, A. Chandra, and L.S. Turng, *Int. Polym. Proc*., **22**, 436 (2007).
46. M.L. Addonizio, E. Martuscelli, and C. Silvestre, *Polymer*, **28**, 183 (1987).
47. H. Nam, P. Maiti, M. Okamoto, T. Kotaka, T. Nakayama, M. Takada, M. Ohshima, A. Usuki, N. Hasegawa, and H. Okamoto, *Polym. Eng. Sci*., **42**, 1907 (2002).
48. H.E. Naguib, C.B. Park, N. Reichelt, and U. Panzer, *Polym. Eng. Sci*., **42**, 1481 (2002).
49. S.T. Lim, Y.H. Hyun, C.H. Lee, and H.J. Choi, *J. Mat. Sci. Lett*., **22**, 299 (2003).
50. T. Li, L.S. Turng, S. Gong, and K. Erlacher, *Polym. Eng. Sci*., **46**, 1419 (2006).
51. X.D. Li, H.S. Gao, W.A. Scrivens, Dl L. Fei, V. Thakur, M.A. Sutton, A.P. Reynolds, and M.L. Myrick, *Nanotechnology*, **19**, 2020 (2005).
52. H. Chen, M. Wang, Y. Lin, C.M. Chan, and J. Wu, *J. Appl. Polym. Sci*., **106**, 3409 (2007).
53. P. Yuan, P.D. Southon, Z. Liu, M.E.R. Green, J.M. Hook, S.J. Antill, and C.J. Kepert, *J. Phys. Chem. C*, **112**, 15742 (2008).
54. K.P. Nicolini, C.R.B. Fukamachi, F. Wypych, and A.S. Mangrich, *J. Colloid. Interf. Sci*., **338**, 474 (2009).
55. C. Li, J. Liu, X. Qu, and Z. Yang, *J. Appl. Polym. Sci*., **112**, 2647 (2009).
56. P. Pasbakhsh, H. Ismail, M.N.A. Fauzi, and A.A. Bakar, *Polym. Test*., **28**, 548 (2009).
57. S. Rooj, A. Das, V. Thakur, R.N. Mahaling, A.K. Bhowmick, and G. Heinrich, *Mater. Design*., **31**, 2151 (2010).
58. S. Deng, J. Zhang, and L. Ye, *Compos. Sci. Technol*., **69**, 2497 (2009).
59. R.B. McClurg, *Chem. Eng. Sci*., **59**, 5779 (2004).
60. L.J. Lee, C. Zheng, X. Cao, X. Han, J. Shen, and G. Xu, *Compos. Sci. Technol*., **65**, 2344 (2005).
61. S. Bruzaud and A. Bourmaud, *Polym. Test*., **26**, 652 (2007).
62. S. Mohanty and S.K. Nayak, *Polym. Compos*., **31**, 1194 (2009).
63. S. Wang, C. Song, G. Chen, T. Guo, J. Liu, B. Zhang, and S. Takeuchi, *Polym. Degrad. Stab*., **87**, 69 (2005).
64. S. Suprakas, Y. Kazunobu, O. Masami, and U. Kazue, *Nano. Lett*., **2**, 1093 (2002).
65. V. Kumar, *Cell. Polym*., **12**, 207 (1992).
66. R. Masirek, Z. Kulinski, D. Chionna, E. Piorkowska, and M.J. Pracella, *J. Appl. Polym. Sci*., **105**, 255 (2007).
67. M. Yasuniwa, S. Tsubakihara, Y. Sugimoto, and C. Nakafuku, *J. Polym. Sci. Part B: Polym. Phys*., **42**, 25 (2004).
68. Y. Wang, S.S. Funari, and J.F. Mano, *Macromol. Chem. Phys*., **207**, 1262 (2006).
69. S. Singh and A.K. Mohanty, *Compos. Sci. Technol*., **67**, 1753 (2007).
70. H.E. Naguib, C.B. Park, and P.C. Lee, *J. Cell. Plast*., **39**, 499 (2003).
71. M. Pracella, D. Chionna, I. Anguillesi, Z. Kulinski, and E. Piorkowska, *Compos. Sci. Technol*., **66**, 2218 (2006).
72. P. Bordes, E. Pollet, and L. Avérous, *Prog. Polym. Sci*., **34**, 125 (2009).
73. O.S. Gabizlioglu, H.W. Beckham, A.S. Argon, R.E. Cohen, and H.R. Brown, *Macromolecules*, **23**, 3968 (1990).
74. A.S. Argon, R.E. Cohen, O.S. Gabizlioglu, H.R. Brown, and E.J. Kramer, *Macromolecules*, **23**, 3975 (1990).
75. S. Wong, R.A. Shanks, and A. Hodzica, *Macromol. Mater. Eng*.. **289**, 447 (2004).
76. S. Pavlidou and C.D. Papaspyrides, *Prog. Polym. Sci*., **33**, 1119 (2008).
77. D.I. Collias and D.G. Baird, *Polym. Eng. Sci*., **35**, 1167 (1995).
78. S. Suprakas and B. Mosto, *Prog. Mater. Sci*., **50**, 962 (2005).
79. X.D. Li, H.S. Gao, W.A. Scrivens, D.L. Fei, X.Y. Xu, M.A. Sutton, A.P. Reynolds, and M.L. Myrick, *Nanotechnology*, **15**, 1416 (2004).
80. A. Kramschuster, S. Gong, L.S. Turng, T. Li, and T. Li, *J. Biobased. Mater. Bioenergy*., **1**, 37 (2007).

 DOI 10.1002/pen